The Spectroscopy of InSe Nanoparticles

Shuming Yang and David F. Kelley*

Division of Natural Sciences, University of California, Merced, P.O. Box 2039, Merced, California 95344

Received: February 7, 2005; In Final Form: April 3, 2005

The synthesis of several different sizes of InSe nanoparticles from organometallic precursors is reported. These particles are characterized by transmission electron microscopy, electron diffraction, and optical spectroscopy. The electron diffraction results and optical properties indicate that these particles are two-dimensional disks, consisting of single Se−In−In−Se tetralayer sheets. The absorption spectra indicate strong quantum confinement along the *z* axis and, for the smaller particles, in the *x*,*y* plane. The *z*-axis quantum confinement may be quantitatively understood in terms of the band structure of bulk InSe. The results indicate that the *z*-axis quantum confinement reverses the order of the direct and indirect transitions in the case of the largest particles. The smaller particles exhibit strong, polarized fluorescence, and the fluorescence polarization may also be understood in terms of the band structure of bulk InSe.

Introduction

Layered semiconductors are of great interest largely because they have optical and electronic properties that are highly anisotropic. The III−VI compounds, such as InSe and GaSe, are layered semiconductors in which a primitive layer consists of four atomic planes, Se−M−M−Se (M = In, Ga). The selenium atoms form two-dimensional hexagonally close-packed sheets, giving these crystals their hexagonal structure. The metal atoms are aligned along the *c* axis in every other trigonal prismatic site.[1] The band gap of InSe is about $E_g = 1.24$ eV at room temperature,[2,3] which makes it an attractive material for solar energy conversion. Due to the absence of dangling bonds on the (001) surface, it has the potential to be used for heterojunction device applications with a low density of interface states.[4,5]

There has been a growing interest in the spectroscopic and photophysical properties of semiconductor nanoparticles, also referred to as quantum dots. Despite this interest, relatively few types of semiconductor nanoparticles have electronic, optical, and photophysical properties that are well understood. This is particularly true for the above-mentioned III−VI layered semiconductors. We have recently reported much of the photophysics of GaSe nanoparticles[6−10] and strongly interacting aggregates of these particles.[11,12] Electron diffraction and optical spectroscopy show that GaSe nanoparticles consist of single tetralayer structures (i.e., Se−Ga−Ga−Se sheets). Thus, they have a disklike, two-dimensional morphology and are exactly four atoms thick. This was an expected result, based on elementary chemical bonding considerations. There are strong covalent bonds within the Se−Ga−Ga−Se sheets, while only weak van der Waals forces hold adjacent sheets together. Detailed spectroscopic studies revealed that GaSe nanoparticles have highly anisotropic optical and quantum confinement properties. We also found that, like the bulk materials, these nanoparticles are quite photostable.

InSe has the same crystal structure and similar lattice constants as GaSe, and would be expected to form similar disklike nanoparticles. Previous studies have shown that InSe nanoparticles can be synthesized by pyrolysis of a single molecular precursor (containing indium and selenium) in a coordinating solvent.[13] This procedure results in somewhat polydisperse InSe nanoparticles. In this study, we present more conventional synthetic methods in an attempt to better control the nanoparticle size distributions. InSe nanoparticles are synthesized in a coordinating organic solvent with conventional organometallic precursors, using procedures that are very analogous to those used to produce GaSe nanoparticles. We find that these procedures permit the control of the nanoparticle sizes and size distributions. We also present some basic aspects of the size-dependent electronic structure of the particles, based on absorption spectra and static and time-resolved fluorescence spectroscopy. These results permit the relative energetics of the different particle excited states to be established.

Experimental Section

Materials. Trimethylindium was purchased from Strem Chemicals and used without further purification. Methyllithium, trioctylphosphine (TOP) and trioctylphosphine oxide (TOPO) were purchased from Sigma-Aldrich. Anhydrous ether, tetrahydrofuran, selenium powder, and indium chloride were purchased from VWR. Trioctylphosphine and trioctylphosphine oxide were distilled under vacuum before use.

Trimethylindium/TOP solutions were used in the synthesis of all the different sizes of nanoparticles, and were prepared in the following way. $InCl_3$ (3.0 g, 13.56 mmol) was added in a flask and heated at 80 °C under vacuum for 1 h. The flask was cooled in an ice bath and purged with argon several times. Absolute ether (20 mL) was then injected and 25.4 mL of methyllithium ether solution (1.6 mol/L) was slowly added. Upon completion of this addition the solution was stirred for 2 h. The trimethylindium was pumped off and collected in a liquid nitrogen cooled trap containing 13.5 mL of TOP. The trap was warmed and the ether was then pumped off. The resulting 1 mol/L trimethylindium in TOP solution was stored in a drybox for further use. We find that the characteristics of this solution are identical with those of solutions made with commercial trimethylindium.

Measurements. The size distributions of the different InSe nanoparticle samples were determined with transmission electron

* Address correspondence to this author. E-mail: dfkelley@ucmerced.edu.

10.1021/jp0506686 CCC: $30.25
Published on Web 06/10/2005

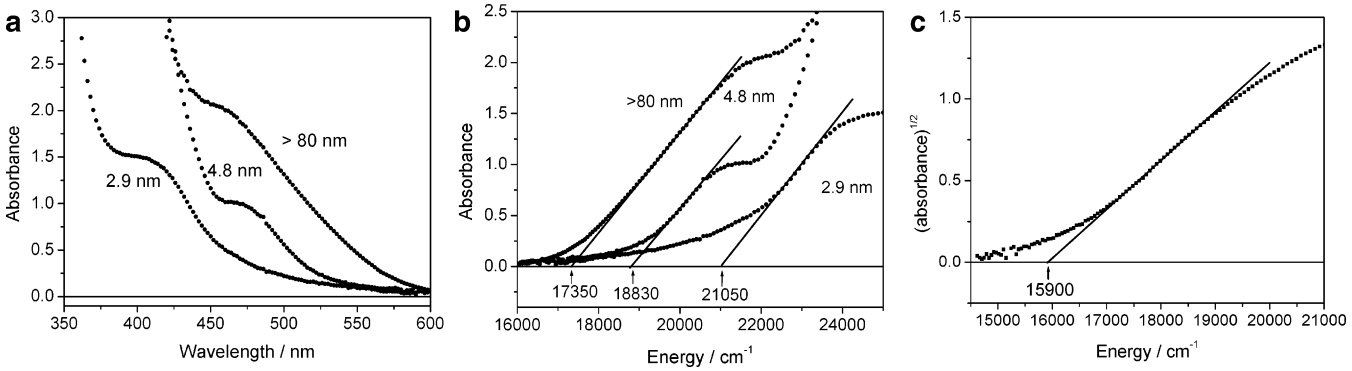

Figure 1. (a) Absorption spectra of 2.9 nm, 4.8 nm, and very large (>80 nm) InSe nanoparticles. (b) Plots of absorbance versus energy for the 2.9 nm, 4.8 nm, and very large particles. Also shown are the extrapolations to zero used to determine approximate band gaps in each case. (c) Plot of the square root of absorbance versus energy for the red edge of the large particle spectrum. Also shown is an extrapolation to zero absorbance.

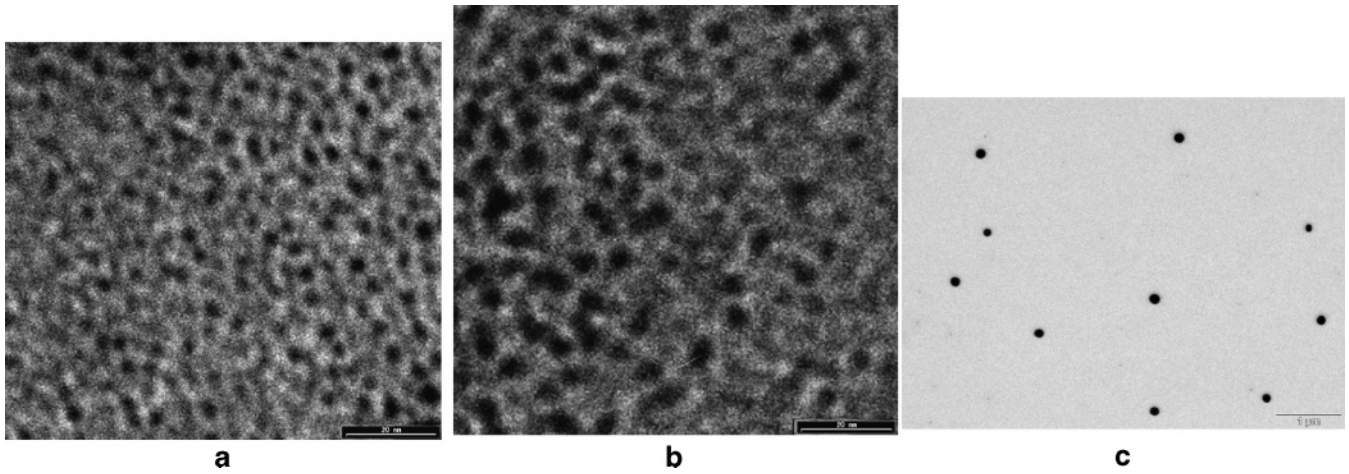

Figure 2. TEM images of (a) 2.9 nm, (b) 4.8 nm, and (c) very large (>80 nm) InSe nanoparticles. Scale bars indicating 20 nm (a and b) and 1 μm (c) are also shown.

microscopy (TEM). This was done with a Phillips CM-12 TEM, operating at 100 kV. A small fraction of the InSe nanoparticle solution is diluted with toluene by a factor of 3, and a drop of the diluted solution is spread over a copper/Formvar grid (300 mesh size). Electron diffraction results were obtained on the same instrument. The absorption spectra were measured in a HP 8452A spectrophotometer. The static fluorescence spectra were obtained on a Spex Fluorolog-3 with a liquid nitrogen cooled CCD detector. Time correlated single photon counting results were obtained with an apparatus described earlier.[11]

Synthesis of 2.9 nm InSe Nanoparticles. All InSe nanoparticle samples were synthesized with schlenck line methods under an argon atmosphere. InSe nanoparticles are synthesized with a method that is a modification of the high-temperature synthesis of CdSe[14] and GaSe[8] nanoparticles. This synthesis is based on the reaction between the organometalic $In(CH_3)_3$ and trioctylphosphine selenium (TOPSe) in a high-temperature solution of trioctylphosphine (TOP) and trioctylphosphine oxide (TOPO). The nucleation and growth of the nanoparticles were monitored by the absorption spectroscopy of small sample aliquots.

The synthesis of 2.9 nm InSe nanoparticles is as follows. Initially, 0.3158 g (4 mmol) of Se, 2.6 g of TOPO, and 3.5 mL of TOP are added to a flask and stirred at 150 °C overnight under an argon atmosphere. The solution is then heated to 250 °C and 1.5 mL of trimethylindium in TOP (1 mol/L) is injected. Upon injection, the temperature drops to 236 °C and the solution is reheated to 248 °C for the growth of the InSe particles. The solution becomes yellow at about 35 min and a shoulder in the absorption spectrum appears at about 410 nm. The reaction is allowed to proceed about 2.5 h and a distinct peak appears at 410 nm, see Figure 1. The solution is then cooled quickly to room temperature. TEM images of this sample are obtained and the size distribution is determined, see Figure 2. Measurement of many particles indicates that the particle diameter is 2.9 ± 0.4 nm (standard deviation).

Synthesis of 4.8 nm InSe Nanoparticles. Se (0.35 g), TOPO (2.5 g), hexyl phosphonic acid (0.045 g), and TOP (3.5 mL) are added to a flask under an argon atmosphere. The mixture is then stirred at 150 °C overnight. The solution is cooled to room temperature and 0.4 mL of trimethylindium in TOP (1 mol/L) is injected. The mixture is then slowly heated to 233 °C for nucleation and subsequent particle growth. The solution becomes yellow and a shoulder in the absorption spectrum appears at 460 nm at about 26 min. The temperature is then maintained at 233 °C for 3.5 h. During this time a more distinct shoulder grows at 475 nm. The solution is then quickly cooled to room temperature. The absorption spectrum of these particles is also shown in Figure 1.

Synthesis of Very Large (>80 nm) InSe Nanoparticles. Se (0.35 g), TOPO (2.5 g), (0.075 g) hexyl phosphonic acid (2.5 g), and TOP (3.5 mL) are added to a flask under an argon atmosphere. The mixture is stirred then at 150 °C overnight. The solution is then cooled to room temperature and 0.4 mL of trimethylindium in TOP (1 mol/L) is injected. The mixture is then slowly heated to 237 °C. It becomes red at about 18 min and a shoulder appears at about 460 nm in the absorption spectrum. The temperature is kept at 237 °C for the growth of

the InSe particles. The entire reaction takes about 5 h and the absorption onset is measured at 580 nm. The solution is then quickly cooled to room temperature. The absorption spectrum of these particles is also shown in Figure 1.

Results and Discussion

Particle Synthesis and Characterization. The basic idea of these syntheses is to obtain InSe nanoparticles with methods similar to those used to prepare GaSe nanoparticles.[8,10] However, the reactivities of the indium and gallium precursors are different, and the central challenge of these syntheses is the control of the reactivity with respect to particle nucleation and growth. The synthesis of monodisperse small particles requires a rapid burst of nucleation, followed by relatively slow particle growth. In general, we find that the presence of TOPO and especially alkyl phosphonic acids inhibits both the nucleation and growth processes. Thus, small (2.9 nm diameter) particles are synthesized by the injection of $In(CH_3)_3$/TOP into a hot solution of TOP/TOPO/TOPSe. Nucleation occurs very rapidly, followed by particle growth. This results in a relatively monodisperse distribution of particle sizes. If the solution is allowed to further react, it will eventually undergo Ostwald ripening, resulting in a defocused, polydisperse sample.

The synthesis of larger (4.8 nm) particles requires the production of fewer nuclei. This is accomplished by mixing the reactants together at room temperature in a solution containing 0.7% hexyl phosphonic acid. InSe nuclei are formed as the solution is heated, with the extent of nucleation controlled by the presence of the hexyl phosphonic acid. Since there are fewer nuclei, subsequent growth results in fewer, larger particles. Addition of larger amounts of hexyl phosphonic acid further inhibits nucleation, permitting the synthesis of very large particles.

Absorption spectra of small (2.9 nm), intermediate (4.8 nm), and very large (>80 nm) InSe nanoparticles are shown in Figure 1a. The corresponding TEM images are shown in Figure 2. Analysis of the size distribution indicates that the standard deviation is about 15% for the case of the 2.9 and 4.8 nm particles. Electron diffraction results on the 4.8 nm and large particles are similar to those obtained for single tetralayer GaSe nanoparticles. Specifically, they show the (1,0,0) and (1,1,0) reflections, while (1,0,2), (1,0,4), (1,1,2), etc. reflections are absent. This indicates that both types of nanoparticles have the same two-dimensional, single tetralayer morphologies. This is exactly what one would expect. The tetralayers are held together by covalent bonds, but are held to each other by much weaker van der Waals forces.

Size-Dependent Absorption Spectra. Bulk InSe has a room temperature absorption onset at 1.24 eV (10 000 cm^{-1} or 1 000 nm).[2] The onsets of the spectra in Figure 1 are shifted into the 450−600 nm region, and therefore show considerable quantum confinement. Approximate absorption onsets for each size particle may be determined from graphs of absorbance plotted as a function of energy, Figure 1b. One of the central questions about the absorption spectra is regarding the nature of the lowest energy transition in terms of the initial and final momentum states. In the case of bulk InSe, the top of the valence band and the bottom of the conduction band are both at Γ and the lowest energy transition is therefore momentum allowed; it is a "direct" transition.[2,3] A slightly higher (750 cm^{-1}) local minimum of the conduction band is at the M point and the corresponding Γ → M transition is a much less intense, momentum-forbidden "indirect" transition.[15] The momentum selection rule breaks down as the particles get smaller. As any particle becomes smaller, the momentum vector, which defines the band structure of the crystal, becomes less well defined. In sufficiently small nanoparticles, the wavelength and hence momentum associated with specific standing waves (symmetry points in the Brillouin zone) are not well defined and the momentum selection rule is relaxed. These two-dimensional nanoparticles are extremely thin (four atoms) and this is particularly true of the *z*-axis symmetry points; it makes little sense to refer to standing waves when the distance over which the wave is defined is one-half of the shortest wavelength. The situation is less severe in the *x*,*y* plane. Particles range from about 8 to over 200 unit cells in diameter, and this is a sufficient distance for the wavelength of a standing wave to be reasonably well defined. Thus, we expect that in the case of the largest particles, there will be little mixing of momentum states in the *x*,*y* plane. The M point is in the *x*,*y* plane and the Γ → M transition will have low intensity. More mixing will occur in smaller particles and the distinction between direct and indirect transitions starts to break down. This phenomenon has been extensively studied, primarily in the context of porous silicon.[16,17] The above breakdown of momentum selection rules notwithstanding, the zeroth order description of the electron and hole states in terms of symmetry points in the first Brillouin zone is very useful. Furthermore, despite some amount of mixing, the nodal properties of the electron and hole wave functions are of central importance in understanding the nanoparticles spectroscopy and we will elucidate this (size dependent) behavior below.

Quantum confinement effects involve energies that are much larger than the Γ−M conduction band energy separation in bulk InSe and there is no a priori way to know whether the lowest point of the conduction band in these particles would be at Γ or M, i.e., the transition could be either direct or indirect. In principle, the functional dependence of the absorbance on energy near the band edge could be used to determine the nature of the lowest energy transition. However, the presence of a finite distribution of particles sizes makes this analysis problematic for the 2.9 and 4.8 nm particles. This determination will be made based on relative oscillator strength results (discussed below), and we will only estimate the band gaps from the results presented in Figure 1b. Absorbance is plotted versus energy and the extrapolation to zero absorbance is used to estimate the band gap. Direct (momentum allowed) transitions are typically much more intense than indirect (momentum forbidden) transitions. As a result, the direct transitions are expected to dominate these plots, and the extrapolations give reasonable estimates for the direct transition energies. (This is a slightly different approach than that used in our initial study of GaSe nanoparticles,[10] but yields similar results.) The 2.9 and 4.8 nm particles show absorption onsets at 21 050 (475 nm) and 18 830 cm^{-1} (531 nm), respectively.

The situation is somewhat different for the largest particles. The Bohr radius of an exciton in InSe is about 5 nm and the largest particles are expected to exhibit very little *x*,*y*-plane quantum confinement.[2] The height of these single tetralayer particles is much less than the Bohr radius, and there is considerable *z*-axis quantum confinement. However, all of the particles have the same height, giving a constant amount of *z*-axis quantum confinement. As a result, the finite distribution of particle sizes is not expected to broaden the absorption onset of the largest particles. We will show (below) that based on band structure calculations, the lowest energy transition in the largest particles is expected to correspond to an indirect band gap. We suggest that this transition is responsible for the weak,

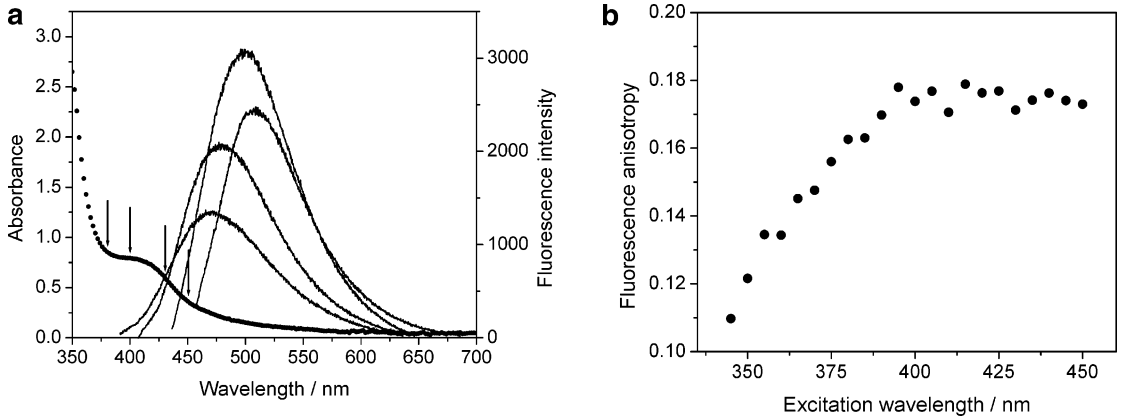

Figure 3. (a) Absorption spectrum and fluorescence spectra of 2.9 nm particles following excitation at 380, 400, 430, and 450 nm (indicated by arrows). (b) Plot of the fluorescence anisotropy as a function of the excitation wavelength for 2.9 nm particles.

low-energy tail observed in the absorption spectrum. The magnitude of the indirect gap may be estimated from a plot of (absorbance)$^{1/2}$ versus energy,[18] as shown in Figure 1c. A value of 15 900 cm^{-1} for the indirect band gap is obtained. Most of the absorbance is due to the far more intense direct (momentum allowed) transition, and an approximate value for its onset (consistent with the values obtained for the smaller particles) is obtained from the extrapolation in Figure 1b. However, absorption into the low-energy indirect transition affects this extrapolation and we conclude that the direct transition may be at somewhat higher energy than the 17 350 cm^{-1} intercept.

In addition to the lowest energy onsets, Figure 1 shows that in each case, a more intense transition is observed further to the blue. For example, the 2.9 nm particles show a low energy transition having an inflection at about 440 nm and a higher energy transition at about 360 nm. We will first discuss the assignment of these transitions in terms of the valence and conduction bands. This will be followed by a discussion of the direct versus indirect nature of the transitions and the quantum confinement effects.

Fluorescence Polarization Measurements. Assignment of the transitions observed in the absorption spectra is facilitated by fluorescence polarization measurements. Since the small particles are the only ones that are strongly fluorescent we will primarily discuss this case. The fluorescence spectra of the 2.9 nm particles following excitation at several different wavelengths are shown in Figure 3a. This fluorescence is polarized and the polarization reveals much about the assignment of these excited states. The fluorescence polarization is characterized by the anisotropy, r, given by[19]

$$r = (I_{\text{par}} - I_{\text{perp}})/(I_{\text{par}} + 2I_{\text{perp}}) = {}^1/_5(3\cos^2\theta - 1)$$

where I_{par} and I_{perp} are the fluorescence intensities polarized parallel and perpendicular to the polarization of the excitation light, respectively, and θ is the angle between the fluorescence and excitation transition oscillators. Several limiting cases are of interest. The case of collinear excitation and fluorescence oscillators results in the largest possible anisotropy for an incoherent process, 0.40. Similarly, the case of coplanar excitation and fluorescence oscillators requires integration over the plane and gives an anisotropy of 0.10. If the excitation and fluorescence oscillators are at 90° angles, an anisotropy of −0.20 is obtained. Figure 3b shows a plot of the fluorescence anisotropy as a function of excitation wavelength. (The anisotropies are essentially constant across the fluorescence spectrum, i.e., they are independent of detection wavelength.) Excitation of the lowest energy transition ($\lambda > 400$ nm) results in a large positive anisotropy, independent of excitation wavelength. This anisotropy has a value of about 0.18. This is greater than 0.10, the value associated with coplanar absorption and fluorescence oscillators, and we conclude that this fluorescence can only result from the excitation and fluorescence oscillators being collinear or the same linear oscillator. With the disklike geometry of these nanoparticles, this transition is assigned to excitation and fluorescence occurring along the z axis, perpendicular to the plane of the nanoparticle. Consistent with the polarization results in bulk InSe,[3] the low-energy absorption may be assigned to excitation of the bandedge state. Fluorescence occurs from this state and/or other states that derive oscillator strength from it. At shorter wavelengths ($\lambda < 380$ nm), some of the excitation goes into the higher energy oscillator and smaller fluorescence anisotropies are obtained. This indicates that the higher energy transition is polarized in the x,y plane of the nanoparticles. Similar behavior is observed for the 4.8 nm particles. Fluorescence from the largest particles is sufficiently weak that useable anisotropy results cannot be obtained. The above results can be understood in terms of band structure and spectroscopy of bulk InSe.[15,20−22] (Although the crystal structure of a single tetralayer has D_{3h}^1 symmetry, we will discuss the electronic states in terms of D_{6h}^4 notation, because that is what usually appears in the literature. The conclusions are the same for D_{6h}^4 and D_{3h}^1 symmetries.[23]) In bulk InSe the lowest energy transition is at Γ ($\Gamma_4^- \rightarrow \Gamma_3^+$) and is z polarized. At somewhat higher energy there is an x,y-polarized transition from a lower level of the valence band to the bottom of the conduction band ($\Gamma_6^- \rightarrow \Gamma_3^+$). We make an analogous assignment here: the lower and higher energy transitions are due to excitation from the Γ_4^- and Γ_6^- valence band levels, respectively, to the bottom of the conduction band. This indicates that despite quantum confinement effects, the energy of the Γ_6^- state remains below that of the Γ_4^- state in these nanoparticles.

Quantum Confinement Effects. The size-dependent absorption and fluorescence spectra of these particles can be qualitatively understood in terms of the two-dimensional nature of these particles. The blue shift of the absorption spectrum occurs because of quantum confinement along the z axis and in the x,y plane. Since all of the particles are exactly four atoms thick, the extent of z-axis quantum confinement is constant. In contrast, the extent of x,y-plane quantum confinement varies with the particle size. The simplest possible way in which the extents of z and x,y quantum confinement can be analyzed is using an effective mass (EM), particle in a cylinder model. In this model, the cylindrical symmetry of the particle results in the electron

and hole wave functions separating into z and x,y functions. Specifically,

$$\Psi_{mnp}(r,\varphi,z) = N_{nm}J_m(\alpha_{mn}r/R)\exp(im\varphi)\sin(p\pi z/H)$$

where R is the particle radius, H is the particle height, J_m is an mth order Bessel function, α_{mn} is the nth root of a Bessel function of order m, N_{mn} is a normalization factor, and p is an integer. From ref 24 we know that $N_{nm} = (2/\pi H)^{1/2}(1/R)(1/J_{m+1}(\alpha_{mn}))$.

The electron and hole energy levels are given by

$$E_{m,n,p} = \frac{p^2\hbar^2\pi^2}{2m_{e(h)}{}^{z}H^2} + \frac{\hbar^2\alpha_{mn}{}^2}{2m_{e(h)}{}^{xy}R^2}$$

where $m_{e(h)}{}^{xy}$ and $m_{e(h)}{}^{z}$ are the electron (hole) effective masses in the x,y plane and along the z axis, respectively, and m, n, and p are quantum numbers. The x,y and z designations for the effective masses reflect the fact that these quantities are highly anisotropic, i.e., they are different for motions in the plane and perpendicular to the plane of the nanoparticle. The total (electron plus hole) quantum confinement of the observed transitions is given by the sum of the electron and hole zero point energies plus a Coulombic term. The electron/hole Coulombic interaction energy may be evaluated through a first-order perturbation approach. The interaction potential is obtained by integrating the electrostatic force. We define

$$V_0(x) = \int_0^x F(x')\,dx'$$

where

$$F(x) = (1/x^2)\frac{\int_0^x (J_0(\alpha_{01}x'))^2 x'\,dx'}{\int_0^1 (J_0(\alpha_{01}x))^2 x\,dx}$$

The resulting electron/hole interaction is obtained from the above integrals and is

$$V_{e(h)} = (Q^2/4\pi\epsilon_0\epsilon)(1/R)\langle J_0(\alpha_{01}x)|V_0(x)|J_0(\alpha_{01}x)\rangle = -1.12(Q^2/4\pi\epsilon_0\epsilon)(1/R)$$

where Q is the electronic charge and ϵ is the dielectric constant of InSe, ≈ 9.[2]

The electronic transition energy is therefore given by

$$E_0 = E_{bulk} + \frac{\hbar^2\pi^2}{2H^2}\left(\frac{1}{m_e{}^{z}} + \frac{1}{m_h{}^{z}}\right) + \frac{\hbar^2\alpha_{01}{}^2}{2R^2}\left(\frac{1}{m_e{}^{xy}} + \frac{1}{m_h{}^{xy}}\right) - \frac{1.12Q^2}{4\pi\epsilon_0\epsilon R} \quad (1)$$

where E_{bulk} is 1.24 eV (10 000 cm^{-1}) for room temperature InSe and α_{01} has a numerical value[25] of 2.405. Equation 1 indicates that the Coulombic term may be added onto the observed transition energies and the resulting corrected energies may be plotted versus $1/R^2$. The intercept of this plot is the bulk band gap plus the z-axis quantum confinement energy. Such a plot is shown in Figure 4, and a reasonable linear fit with $1/R^2$ is obtained. The intercept of this plot, 17 490 cm^{-1}, corresponds to a z-axis quantum confinement energy of 7490 cm^{-1}. As discussed above, the absorption is dominated by the direct transition and this value applies to the direct band gap. The energy of the indirect band gap for the large particles (Figure 1c) is also shown in Figure 4. As the particle size decreases, the absorption onset shifts further to the blue because of additional quantum confinement in the x,y plane. The roles of z and x,y quantum confinement are dealt with separately, below.

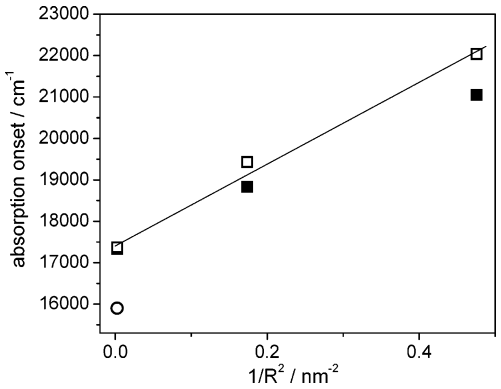

Figure 4. Plots of the measured direct band gap as a function of 1/(particle radius)^2 (solid squares), the direct band gap corrected by the Coulombic term (solid circles), and the indirect band gap of the large particles (open circle). Also shown is a line through the points having an intercept of 17 400 cm^{-1} and a slope of 10 100 cm^{-1}/nm^{-2}.

The diameter of the large particles (>80 nm) is much larger than the InSe Bohr radius (5 nm), the result being that these particles exhibit large z-axis quantum confinement but very little x,y quantum confinement. The direct and indirect band edges, and hence the absorption spectrum of the large particles, can be understood in terms of measurements on bulk InSe and band structure calculations.[15,20−22] Bulk InSe has significant interaction between the tetralayer sheets and z-axis quantum confinement can be thought of as being due to the loss of this interaction. Interlayer interactions split the Γ_4^- and Γ_1^+ valence band states and the Γ_3^+ and Γ_2^- conduction band states. The extent of z-axis quantum confinement can be assessed by comparing the calculated conduction and valence band energies at the Γ (the direct band gap) and A (where the interlayer interaction is zero) symmetry points. The energy differences are 4875 cm^{-1} in the valence band and 3810 cm^{-1} in the conduction band, with the total, 8685 cm^{-1}, being the calculated z-axis, direct band gap quantum confinement energy.[20] However, the presence of a $\Gamma \rightarrow$ M indirect transition complicates the spectroscopy of InSe nanoparticles, and insight into the energetics of this transition comes from optical measurements on γ-InSe and calculations. Bulk InSe exists in β- and γ-polytypes, having hexagonal and rhombohedral lattices, respectively. The difference is in the stacking of the tetralayer sheets, and the two forms have very similar energetics. As a result, measurement on γ-InSe can be used to establish the energetics of the band structure calculated for the $D_{6h}{}^4$ crystal structure (β-InSe). The energy difference between the direct and indirect transitions has been accurately determined in the case of γ-InSe, and the indirect transition is 750 cm^{-1} higher.[15] This energy difference is strongly dependent on the extent of interlayer interactions. The calculated[20] conduction band interlayer splitting at M (M_3^+ versus M_4^-) is relatively small, about 3000 cm^{-1}. So, the indirect band gap z-axis electron quantum confinement energy may be taken to be about half this value, 1500 cm^{-1}. With the above 750 cm^{-1} bulk $\Gamma-$M energy difference, we get that loss of the interlayer interaction will result in an electron energy at the M point of 2250 cm^{-1} above the bottom of the bulk InSe conduction band. In the absence of interlayer interactions, this puts it below the energy of an electron at Γ by 1560 cm^{-1} (3810 cm^{-1} − 2250 cm^{-1}). It is important to note that these

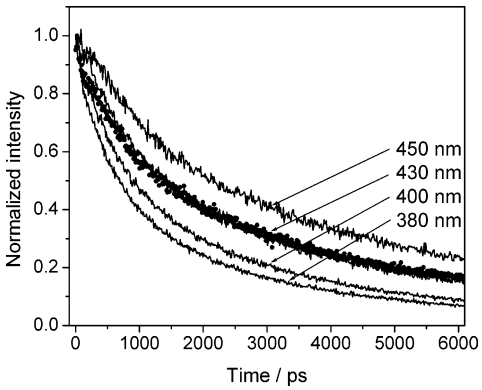

Figure 5. Fluorescence decay kinetics for 2.9 and 4.8 nm particles. The 2.9 nm fluorescence decays (solid curves) are obtained following excitation at 380, 400, 430, and 450 nm. The 4.8 nm fluorescence decay (dotted curve) is obtained following excitation at 450 nm. In all cases the detection wavelength is 500 nm.

calculations indicate that loss of the interlayer interactions reverses the ordering of the Γ and M energies and results in the lowest energy transition being momentum forbidden. The direct transition is calculated to be at about 1560 cm^{-1} higher energy. This is in agreement with the difference in the extrapolated values shown in Figures 2 and 4, supporting the assignments to the indirect and direct transitions. Combined with the 4875 cm^{-1} quantum confinement of the hole, the $\Gamma \rightarrow M$ and $\Gamma \rightarrow \Gamma$ transition energies in large, tetralayer particles are calculated to be about 17 125 and 18 685 cm^{-1}, in reasonable agreement with the 15 900 and 17 490 cm^{-1} experimental values.

The energetic ordering of the $\Gamma \rightarrow \Gamma$ and $\Gamma \rightarrow M$ transitions in smaller particles can be assessed from time-resolved fluorescence and fluorescence quantum yield measurements. These results (discussed below) suggest that the nature of the lowest energy state (direct versus indirect transitions) is size dependent.

Fluorescence Kinetics and Quantum Yields. The above fluorescence polarization results show that the lowest excited state corresponds to the $\Gamma_4^- \rightarrow \Gamma_3^+$ transition, or a transition that through some mechanism (such as vibronic coupling) derives oscillator strength from it. Thus, in all cases, the lowest energy absorption can be assigned to either the direct ($\Gamma_4^- \rightarrow \Gamma_3^+$) or the indirect ($\Gamma_4^- \rightarrow M_3^+$) transition. Fluorescence decay and quantum yield measurements give insight into these assignments and suggest that the ordering of these transitions is particle size dependent. Fluorescence decay times are a function of excitation wavelength, and to a lesser extent, particle size, as shown in Figure 5. (Laser tunability limits the excitation wavelength to ≤450 nm.) Decay times increase with further red excitation, particularly in the 2.9 nm particles. The 4.8 nm particles exhibit very similar decay kinetics following 430 and 450 nm excitation. However, the fluorescence is sufficiently weak following 380 and 400 nm excitation that reliable decay curves could not be obtained. The dependence of decay times on excitation wavelength can be made more quantitative by comparing the areas under the decay curves, normalized to unity at $t = 0$. The decay curves are nonexponential, and with this normalization, the area under the curve is a measure of the "average" decay time. Average decay times are seen to increase with further red excitation, as shown in Figure 6. A similar effect has been observed for GaSe nanoparticles,[8] and is due to additional nonradiative relaxation pathways (probably carrier trapping) available at higher energy. The emission decay time correlates with the observed fluorescence quantum yields, as is also shown in Figure 6. Longer decay times give similarly higher quantum yields. This suggests that all of the particles of any given size have similar oscillator strengths.

The most important point resulting from the data in Figure 6 comes from the comparison of the fluorescence quantum yields of the 2.9 and 4.8 nm particles (Figure 6a,b). This comparison reveals a very strong particle size dependence. The 2.9 nm particles exhibit high fluorescence quantum yields. The exact values vary from sample to sample, and in some cases approach 40%. Quantum yields in the range of 12−25% (Figure 6) are typical. In contrast, the 4.8 nm particles consistently exhibit very small quantum yields, typically less than 0.5%, which is a factor of about 50 lower than the 2.9 nm particles. We emphasize that this difference is not due to differences in quenching rates. Figure 5 shows roughly comparable fluorescence decay kinetics for both sizes of nanoparticles. For example, following 430 nm excitation, both 2.9 and 4.8 nm particles exhibit an approximate decay time (e^{-1} times) of 2.5 ns. The excitation wavelength-dependent results also suggest that the quantum yield difference between the 2.9 and 4.8 nm particles is not due to larger Γ−M mixing in the smaller particles. If this were the case, further red excitation (which excites the largest particles in the size distribution) would result in weaker fluorescence. Figure 6 shows that the opposite is observed. The quantum yield and fluorescence decay results suggest the emitting states are different for the two particle sizes. In the case of the small particles the high fluorescence quantum yield suggests that the emitting state is the same as the absorbing state and is allowed. In contrast, in the case of the 4.8 nm particles, the low quantum yield suggests that the emitting state has very little oscillator strength. This trend with particle size continues and the largest (>80 nm) particles are almost completely nonfluorescent. There are two possible assignments for this trend. First, that in the larger particles the (weakly) emitting state is localized, a trap

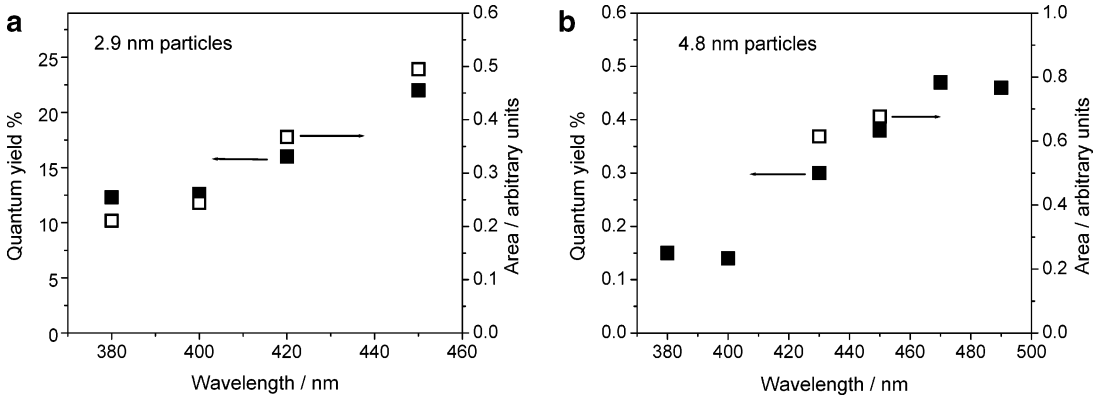

Figure 6. (a) Fluorescence quantum yields (solid squares) and areas under the fluorescence decay curves (open squares) for 2.9 nm particles as a function of excitation wavelength. (b) Same as part a, except for 4.8 nm particles.

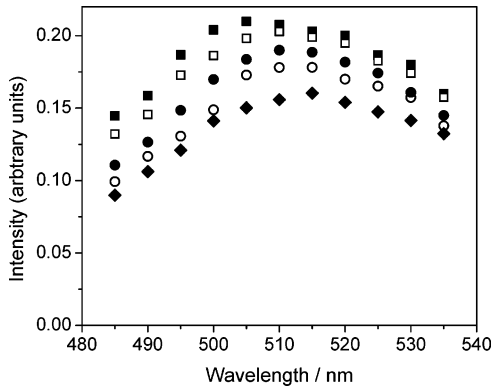

Figure 7. Reconstructed time-resolved fluorescence spectra for 4.8 nm particles, following 450 nm excitation. Spectra are shown at times of 0 ps (solid squares), 12 (open squares), 35 (solid circles), 105 (open circles), and 295 ps (solid diamonds). The fluorescence maximum shifts from approximately 505 to 515 nm in this time interval.

state. Second, that the large particle emitting state is a delocalized electronic state corresponding to an indirect band gap. The first possibility cannot be ruled out based on the results presented here, but several considerations suggest that it is unlikely. This assignment would require that the 4.8 nm and very large particles have a much higher density of trap states than the 2.9 nm particles. This seems unlikely because these results are very reproducible and the synthetic conditions used to obtain the different sizes of particles are very similar. Alternatively, the second possibility would require that the energy of the indirect band edge be at a lower energy than the direct band edge for all but the smallest particles, in which the opposite is true. This latter assignment is consistent with the band structure calculations discussed above, which place the direct band edge 1560 cm^{-1} above the indirect edge in the large particles. This assignment requires that the 4.8 nm and large particles have qualitatively similar energetics; they both have a lowest indirect band edge. In contrast, the 2.9 nm particles are strongly fluorescent, indicating that the lowest transition is at Γ and therefore allowed. The indirect transition must be at a higher energy in these particles. We also suggest that the energies of the direct and indirect transitions are quite close in the case of the 2.9 nm particles, and the reversal of these energies occurs at only slightly larger sizes. In this case, some of the small particles in the distribution will have a direct lowest energy transition and some will not, as a result of a finite distribution of particle sizes. The fraction that do will change with small variations in the average particle size and the sample polydispersity. We observe that some samples of about this size are more fluorescent than others, and we suggest that small variations in the size distribution and hence ordering of these states may be the reason for this.

The above assignments are consistent with time-resolved fluorescence spectral reconstruction results. In the case of the 4.8 nm particles, excitation is primarily to the direct transition (it has most of the oscillator strength) and is followed by relaxation to the weakly fluorescing indirect state. Prior to this relaxation, the fluorescence is predicted to be more intense and further to the blue. Consistent with this explanation, the 4.8 nm fluorescence kinetics show a small spike coincident with zero time, particularly at wavelengths blue of the static fluorescence maximum. However, this effect can most clearly be seen in the reconstructed time-resolved fluorescence spectra. These fluorescence spectra can be reconstructed from the static spectra and wavelength dependent fluorescence kinetics. Fluorescence kinetics are obtained at 5 nm intervals and normalized such that the area under each decay curve is proportional to the static fluorescence intensity at that wavelength. Low-resolution (5 nm) time-resolved fluorescence spectra may then be obtained directly from these decay curves. An example of these spectra is shown in Figure 7. The fluorescence maximum may be obtained by interpolating these points with a fourth order polynomial, and finding the polynomial maximum. The results of this procedure for the 2.9 and 4.8 nm particles are shown in Figure 8. The fluorescence spectra of the 4.8 nm particles show a rapid, greater than 10 nm red shift that is absent in the case of the 2.9 nm particles. The time resolution of time correlated single photon counting is about 40 ps, and this shift is limited by the time resolution of the apparatus. The magnitude of the spectral shift reflects the energy loss associated with relaxation and the results in Figure 8 indicate the spectral shift is on the order of 450 cm^{-1}. We note that because this measurement is limited by the response time of the instrument, the actual magnitude of the spectral relaxation could be considerably larger. However, this result suggests that the magnitude of the energy relaxation must be at least on the order of 450 cm^{-1}. The magnitude of the spectra shift is consistent with the low fluorescence intensity observed in the case of the 4.8 nm particles. If the energy relaxation were less than or on the order of 200 cm^{-1} (thermal energy at room temperature) both the high energy, optically allowed, and lower energy, forbidden, states would have significant populations when in thermal equilibrium. In this case, a significant amount of fluorescence would be from the higher energy allowed transition, and a large change in the fluorescence intensity and spectral maximum would not be observed.

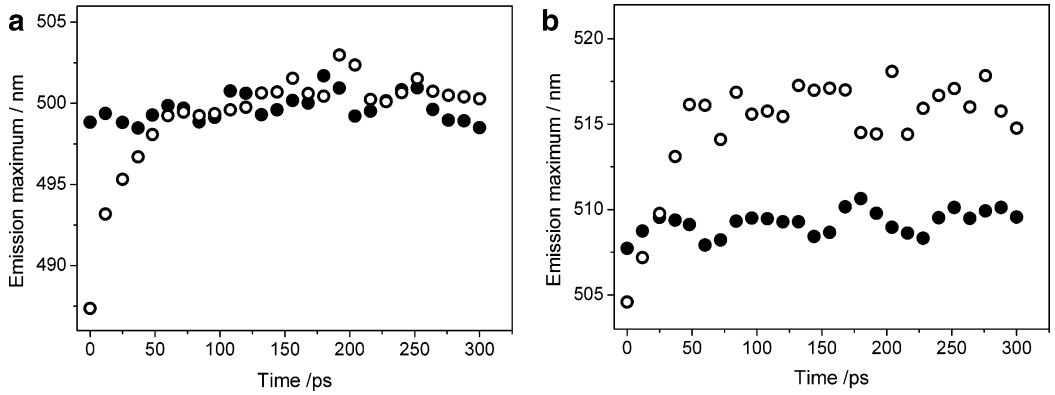

Figure 8. Plots of fluorescence maxima as a function of time for 2.9 nm (solid circles) and 4.8 nm (open circles) particles, following excitation at (a) 430 and (b) 450 nm. These results are obtained from reconstructed fluorescence spectra such as those shown in Figure 7, as described in the text.

Comparison with an Effective-Mass Treatment. It is possible to attempt to quantitatively analyze the size-dependent energetics in Figure 4 in terms of the simple effective mass model described above. In the simplest form, this amounts to the use of eq 1 to fit the size-dependent direct band gaps, with the appropriate values of the effective masses. The effective masses are known[26−29] and have values (in units of electron mass) of 0.081, 2.5, 0.131 and 1.0 for m_e^z, m_h^z, m_e^{xy}, and m_h^{xy}, respectively. The effective masses for the indirect transition have not been reported, so we will confine our discussion to the direct transition. The observed *z*-axis quantum confinement energy ($\approx$7500 cm^{-1} at Γ) can be compared with the value of $\hbar^2\pi^2/2H^2(1/m_e^z + 1/m_h^z)$. Similarly, the observed slope ($\approx$10 100 cm^{-1}/nm^{-2}) of the Coulomb-corrected energies may be compared to the value of $\alpha_{01}^2\hbar^2/2(1/m_e^{xy} + 1/m_h^{xy})$. In addition to treating the particle energies through their effective masses, this model makes several other approximations. The nanoparticles are taken to have cylindrical symmetry, which is probably a pretty good approximation. A more serious approximation is that eq 1 tacitly assumes that the potential well is infinitely deep. Most importantly, it is an effective mass treatment and assumes that the bands are parabolic. Because of these approximations, we find that the agreement of the observed and effective mass calculated *z*-axis quantum confinement energies is poor. This simple model predicts a very large value for the *z*-axis quantum confinement, about a factor of 8 larger than the observed value. Part of the problem is that the model assumes that the electron and hole are confined in a cylinder having infinite potential walls. This is not a very good approximation, and charge density is expected to "spill over" these walls, particularly along the *z* axis. A finite, realistic well depth can be readily incorporated into these calculations.[30] This decreases the discrepancy, but the predicted *z*-axis quantum confinement is still about a factor of 2 larger than the observed value. We conclude the effective mass approximation provides only a semiquantitative description of the *z*-axis quantum confinement.

These particles are much larger in the *x*,*y* dimensions than along the *z* axis. Because of this, both the parabolic band effective mass approximation and the infinite potential approximation might be expected to give a better description of *x*,*y* quantum confinement. Evaluation of the *x*,*y* quantum confinement term gives a $1/R^2$ coefficient of 15 250 cm^{-1}/nm^2. The slope of the plot in Figure 4 gives an experimental value of 10 100 cm^{-1}/nm^2, about a factor of about 1.5 below the value derived from the effective mass model. It is also possible to calculate the extent of *x*,*y* quantum confinement by using a realistic well depth. This calculation is analogous to the one-dimensional calculation with a finite well depth[30] and is outlined in another publication.[31] This diminishes the size of the error and the calculated value for the 2.9 nm particles is about 24% larger than the observed *x*,*y* quantum confinement. We conclude that the effective mass model significantly overpredicts the extent of *z* quantum confinement, but only slightly overpredicts the extent of *x*,*y* quantum confinement. In both cases, the basic problem is that the bands are not parabolic.[32,33] There are several reasonably close lying conduction bands that interact, reducing the extent of quantum confinement. More accurate treatments have been applied to other types of semiconductor nanoparticles, but as yet, such calculations have not been performed for InSe nanoparticles.

Conclusions

Several conclusions may be drawn from the results presented here.

1. Different sizes of InSe nanoparticles may be synthesized with the methods presented here. The particle sizes are controlled through the chemistry of the reaction mixture and the temperatures at which nucleation and growth take place.

2. InSe nanoparticles are two-dimensional, consisting of single tetralayer (Se−In−In−Se) disks. Sizes from 2.9 to >80 nm may be obtained.

3. Most of the quantum confinement of the largest (>80 nm) and intermediate size (4.8 nm) particles is due to *z*-axis quantum confinement. Although bulk InSe is a direct band gap semiconductor, these particles have an indirect band gap. The reversal of these states can be understood in terms of the InSe band structure.

4. The smallest nanoparticles (2.9 nm) exhibit intense fluorescence, while larger (4.8 and >80 nm) particles exhibit at most very weak fluorescence. Time-resolved measurements indicate that this is due to differences in oscillator strength, rather than fluorescence lifetimes. Also, the fluorescence spectrum of the 4.8 nm (but not 2.9 nm) particles exhibits a rapid (<40 ps) shift to the red immediately following photoexcitation. These results are interpreted in terms of size-dependent quantum confinement effects causing the direct transition to be at lower energy than the indirect transition for the 2.9 nm, but not 4.8 nm or >80 nm particles.

Acknowledgment. This work was supported by grants from the U.S. Department of Energy, grant no. DE-FG03-00ER15037, and from the Army Research Office, grant no. W911NF-04-1-0331.

References and Notes

(1) Levy, F. *Crystallography and Crystal Chemistry of Materials with Layered Structures*; Reidel: Dordrecht, The Netherlands, 1976.
(2) Camassel, J.; Merle, P.; Mathieu, H.; Chevy, A. *Phys. Rev. B* **1978**, *17*, 4718.
(3) Piacentini, M.; Doni, E.; Girlanda, R.; Grasso, V.; Balzarotti, A. *Nuovo Cimento* **1979**, *54B*, 269.
(4) Martinez-Pastor, J.; Segura, A.; Julien, C.; Chevy, A. *Phys. Rev. B* **1992**, *46*, 4607.
(5) Lang, O.; Klein, A.; Pettenkofer, C.; Jaegermann, W.; Chevy, A. *J. Appl. Phys.* **1996**, *80*, 3817.
(6) Chikan, V.; Kelley, D. F. *Nano Lett.* **2002**, *2*, 1015.
(7) Chikan, V.; Kelley, D. F. *J. Chem. Phys.* **2002**, *117*, 8944.
(8) Chikan, V.; Kelley, D. F. *Nano Lett.* **2002**, *2*, 141.
(9) Chikan, V.; Kelley, D. F. *J. Phys. Chem. B* **2002**, *106*, 3794.
(10) Tu, H.; Chikan, V.; Kelley, D. F. *J. Phys. Chem. B* **2003**, *107*, 10389.
(11) Tu, H.; Yang, S.; Chikan, V.; Kelley, D. F. *J. Phys. Chem. B* **2004**, *108*, 4701.
(12) Tu, H.; Mogyorosi, K.; Kelley, D. F. *J. Chem. Phys.* **2005**, *122*, 44709.
(13) Revaprasadu, N.; Malik, M. A.; Carstens, J.; O'Brian, P. *J. Mater. Chem.* **1999**, *9*, 2885.
(14) Peng, X.; Wickham, J.; Alivisatos, A. P. *J. Am. Chem. Soc.* **1998**, *120*, 5343.
(15) Manjón, F. J.; Errandonea, D.; Segura, A.; Muñoz, V.; Tobías, G.; Ordejón; Canadell, E. *Phys. Rev. B* **2001**, *63*, 125330.
(16) Ben-Chorin, M.; Averboukh, B.; Kovalev, D.; Polisski, G.; Koch, F. *Phys. Rev. Lett.* **1996**, *77*, 763.
(17) Takagahara, T.; Takeda, K. *Phys. Rev. B* **1992**, *46*, 15578.
(18) Yu, P. Y.; Cardona, M. *Fundamentals of Semiconductors*; Springer: Berlin, Germany, 2001.
(19) Albrecht, A. *J. Mol. Spectrosc.* **1961**, *6*, 84.
(20) Camara, M. O. D.; Mauger, A.; Devos, I. *Phys. Rev. B* **2002**, *65*, 125206.
(21) Gomes-da-Costa, P.; Dandrea, R. G.; Wallis, R. F.; Balkanski, M. *Phys. Rev. B* **1993**, *48*, 14135.
(22) Ferlat, G.; Xu, H.; Timoshevskii, V.; Blase, X. *Phys. Rev. B* **2002**, *66*, 85210.
(23) Koster, G. F.; Dimmock, J. O.; Wheeler, R. G.; Statz, H. *Properties of the Thirty-Two Point Groups*; M.I.T.: Cambridge, MA, 1963.
(24) Arfken, G. *Mathematical Methods for Physicists*; Academic Press: New York, 1970.

(25) Abromowitz, M.; Stegun, I. A., Eds. *Handbook of Mathematical Functions*; Dover: New York, 1965.

(26) Kress-Rogers, E.; Nicholas, R. J.; Portal, J. C.; Chevy, A. *Solid State Commun.* **1982**, *44*, 379.

(27) Segura, A.; Guesdon, J. P.; Besson, J. M.; Chevy, A. *J. Appl. Phys.* **1983**, *54*, 876.

(28) Williams, R. H.; McCanny, J. V.; Murray, R. B.; Ley, L.; Kemeny, P. C. *J. Phys. C* **1977**, *10*, 1223.

(29) McCanny, J. V.; Murray, R. B. *J. Phys. C* **1977**, *10*, 1211.

(30) Landau, L. D.; Lifshitz, E. M. *Quantum Mechanics*; Pergamon Press: Oxford, UK, 1977.

(31) Tu, H.; Mogyorosi, K.; Kelley, D. F. *Phys. Rev. B* **2005**, submitted for publication.

(32) Efros, A. L.; Rosen, M. *Annu. Rev. Mater. Sci.* **2000**, *30*, 475.

(33) Banin, U.; Lee, C. J.; Guzelian, A. A.; Kadavanich, A. V.; Alivisatos, A. P.; Jaskolski, W.; Bryant, G. W.; Efros, A. L.; Rosen, M. *J. Chem. Phys.* **1989**, *109*, 2306.